Mistiming Death: Modeling the Time-Domain Variability of Tumor Apoptosis and Implications for Molecular Imaging of Cell Death

Seth Gammon[1,a], **Brian J. Engel**[1,a], **Gregory J. Gores**[2], **Erik Cressman**[3], **David Piwnica-Worms**[1], **Steven W. Millward**[1,*]

[1.]Department of Cancer Systems Imaging, UT MD Anderson Cancer Center, Houston, TX

[2.]College of Medicine, The Mayo Clinic, Rochester, MN

[3.]Department of Interventional Radiology, UT MD Anderson Cancer Center, Houston, TX

Abstract

Purpose.—Apoptosis, in the context of cancer, is a form of programmed cell death induced by chemotherapy, radiotherapy, and immunotherapy. As this is a central pathway in treatment response, considerable effort has been expended on the development of molecular imaging agents to non-invasively measure tumor apoptosis prior to quantitative changes in tumor dimensions. Despite these efforts, clinical trials directed at imaging apoptosis by PET, SPECT, and MRI have failed to robustly predict response to treatment with high sensitivity and specificity. Although these shortcomings may be linked to probe design, we propose that the combination of variability in the timing of maximal *in vivo* tumor apoptosis and sub-optimal sampling times fundamentally limits the predictive power of PET/SPECT apoptosis imaging.

Procedures.—Herein, we surveyed the literature describing the time-course of therapy-induced tumor apoptosis *in vivo* and used these data to construct a mathematical model describing the onset, duration, amplitude, and variability of the apoptotic response. Uncertainty in the underlying time of initiation of tumor apoptosis was simulated by Gaussian, uniform, and Landau distributions centered at the median time-to-maximum apoptotic rate derived from the literature. We then computationally sampled these models for various durations to simulate PET/SPECT imaging agents with variable effective half-lives.

Results.—Models with a narrow Gaussian distribution of initiation times for tumor apoptosis predicted high contrast ratios and strong predictive values for all effective tracer half-lives. However, when uncertainty in apoptosis initiation times were simulated with uniform and Landau distributions, high contrast ratios and predictive values were only obtained with extremely long imaging windows (days). The imaging contrast ratios predicted in these models were consistent

[*]To whom correspondence should be addressed: smillward@mdanderson.org.
[a]These authors contributed equally to this work.

Conflict of Interest Statement
None

with those seen in pre-clinical apoptosis PET/SPECT imaging studies and suggest that uncertainty in the timing of tumor cell death plays a significant role in the maximal contrast obtainable. Moreover, when uncertainty in both apoptosis initiation and imaging start times were simulated, the predicted contrast ratios were dramatically reduced for all tracer half-lives.

Conclusions.—These studies illustrate the effect of uncertainty of apoptosis initiation on the predictive power of PET/SPECT apoptosis imaging agents and suggest that long integration times are required to surmount uncertainty in the time domain of this biological process.

Introduction

Programmed cell death (PCD) plays a key role in organ development, normal functioning of the immune system, neonatal survival, and tissue homeostasis[1]. Apoptosis (Type 1 PCD) is triggered by both external (e.g. TRAIL ligand) or internal (e.g. DNA damage) signaling events. Apoptosis is characterized by pyknosis, chromosomal fragmentation, and membrane blebbing[2]. In most cases, apoptosis is the default PCD pathway, although inactivation of this pathway in cancer (e.g. through p53 inactivation) can lead to subsequent engagement of alternate pathways, such as autophagic and necrotic death programs[3].

In cancer, normal apoptotic programming is often inactivated or subverted to permit tumor cells to proliferate in the presence of significant genomic derangement, metabolic crisis, and cellular stress[4]. Most clinical cancer treatments exert their therapeutic effect by tipping the balance between pro- and anti-apoptotic signaling toward induction of the apoptotic death program. While our understanding of the molecular mechanisms of apoptotic cell death has grown significantly since the inception of chemotherapy and radiotherapy, our ability to measure cell death clinically has remained limited to monitoring tumor size after a full course of treatment by non-targeted anatomical imaging (RECIST[5]). One of the central goals of personalized cancer treatment is to determine whether a given therapeutic regimen triggers high levels of tumor cell apoptosis and to adjust treatment in real-time until sufficient tumor death is achieved. Molecular imaging of apoptosis could serve this purpose as a generalized pharmacodynamic imaging biomarker of treatment efficacy and dramatically accelerate the realization of personalized medicine.

Numerous molecular imaging agents have been developed to visualize tumor apoptosis in pre-clinical animal models and can be broadly divided into caspase substrates[6–8], caspase inhibitors (e.g. isatin derivatives)[9–10], phosphatidylethanolamine ligands (e.g. duramycin and cinnamycin)[11] and phosphatidylserine ligands (e.g. Annexin V, the C2A domain of synaptotagmin-1[12] and phosphatidylserine-binding antibodies and peptides[13,14–16]. These agents are typically paired with a fluorophore or radionuclide whose half-life roughly matches the biological half-life of the probe. Thus, most fast clearing peptides and small molecules are labeled with short-lived radionuclides such as fluorine-18 (half-life = 109 min) and most slow clearing proteins/antibodies are paired with long-lived radionuclides such as technetium-99m or indium-111 (half-lives in hours to days) or fluorescence reporters. These allow sampling of tumor apoptosis across time scales ranging from minutes to days.

Despite the diversity of apoptosis molecular imaging probes in the pre-clinical space, there are no molecular imaging technologies available to visualize and quantify tumor apoptosis in the clinic. Clinical trials with Annexin-based SPECT agents in several cancers including breast, head and neck, lung, and lymphoma failed to show robust prediction of response based on imaging shortly after chemotherapeutic or radiation treatment (20–50% increase in tumor uptake)[17]. More recent studies with ICMT-11 likewise showed only a modest contrast ratio between apoptotic and normal tissue and subsequently limited predictive power[18]. Both strategies showed great promise in pre-clinical studies[14, 19], yet struggled to attain the sensitivity and specificity required for clinical decision-making.

The spatial and temporal heterogeneity of therapy-mediated tumor cell apoptosis confounds traditional molecular imaging strategies. Many cancer treatments trigger low-level apoptosis in only a fraction of tumor cells at any given time[20–22]. This phenomenon is linked to the cell cycle, local therapeutic concentration, local partial pressure of oxygen (hypoxia), and tumor clonal heterogeneity[23]. The functional result is heterogeneity of apoptosis following treatment which is further compounded by high background apoptotic activity arising from increased tumor cell turnover[24]. Finally, most therapies require weeks to months in order to generate anatomically detectable response (decreased tumor volume) indicating that apoptosis induction persists over a long period of time. In contrast, most molecular imaging strategies sample the tumor for minutes to hours. This timescale is governed by six probe-related rate constants: perfusion, clearance, isotopic decay, metabolism, activation, and retention.

Because of the significant, robust, and reproducible efforts of the molecular imaging and pathology communities over the past 20 years, a substantial body of data describing *in vivo* tumor apoptotic responses are now available. These new data may enable better reporter design or better selection of apoptosis imaging applications. After reviewing years of IHC data and *in vivo* experiments, we propose that these data indicate that the predictive power of apoptosis imaging is limited not only by the biochemical robustness of the reporters, but also by the underlying temporal uncertainty in the activation of the biological process.

To investigate the potential effects of variability in the initiation of apoptosis and imaging integration time on image contrast and predictive power, a mathematical model of tumor apoptosis was developed based on a survey of the pre-clinical literature. This model was designed to study the imaging properties of cell death reporters on a macroscopic scale based on the spatial resolution of PET/SPECT/CT. Therefore, in the following analysis, tumor refers to the bulk tumor immune microenvironment (TIME) - the heterogeneous mixture of tumor, immune, and stromal cells that individually undergo cell death and contribute to the total signal in the tumor compartment. We simulated variability in initiation of apoptosis using uniform, Gaussian, and Landau probability distributions centered at the median time of maximal apoptotic response from the literature. Predicted contrast ratios and Area Under the Receiver-Operator Curves (AUROCs) were calculated for each model as a function of total integration (imaging) time and compared to observed data in the PET/SPECT apoptosis imaging literature. Finally, variability in imaging start time relative to the initiation of therapy was simulated using the same approach described above to determine the combined effect of variability in apoptosis initiation time and imaging procedure

initiation. Our results predicted that robust molecular imaging of apoptosis is profoundly time-dependent and that long integration (imaging) times are necessary to compensate for uncertainty in apoptosis initiation and imaging start time.

Methods

Model Construction

We surveyed the literature to identify studies where a time course of tumor apoptosis was explicitly determined by *ex vivo* analysis (Figure 1). Acceptable methods to identify and quantitate tumor apoptosis included immunohistochemical staining for cleaved caspase 3/7, TUNEL assay, or tissue morphology (Gold standards). Only studies that provided quantitative measurement of tumor apoptosis were used. The apoptotic response from each study was extracted, normalized to time 0 hrs, and then plotted against time to obtain an integrated apoptotic response curve. From these curves, the full width at half-maximum (FWHM, hours), fold-change at maximum, and time to maximum (hours), were extracted. All data were converted to mean or median ± standard deviation as necessary. Standard error of the mean was converted to standard deviation (SD) by multiplying SEM by the square root of the number of replicates. Interquartile range was converted to SD as described[25]. 95% confidence intervals were converted to SD as described[26]. The resulting data were normalized to baseline values and the features described above were extracted. Although the apoptotic response curves fell into six categories (unimodal, bi-modal, hyperbolic, sigmoidal, exponential, and biphasic – see Figure 2), the majority of studies showed a unimodal response that was used to construct the mathematical model.

Model Analysis

All mathematical models were constructed in Mathematica version 10. Tumor baseline apoptosis was modeled as a low frequency oscillator with a Gaussian distribution of high frequency noise. Induced tumor apoptosis was modeled as a Gaussian response additive to the baseline and constrained to the median fold-change, time to maximum response, and FWHM parameters obtained from the literature survey (Table 1). 2000 apoptosis initiation times were randomly selected from a Gaussian distribution (mean at 48 hours; SD 24 hours), a truncated Gaussian distribution (mean at 24 hours; SD 24 hours), an asymmetric heavy-tailed Landau distribution (mean at 48 hours; sigma = 1) a truncated Landau distribution (mean at 24 hours, sigma = 1), or a random (uniform) distribution. These apoptosis induction times then were utilized to build induced and baseline time series. An unweighted numerical integration was calculated for both the induced and background apoptosis states for durations of 0.5 to 216 hours starting at 24 hours. This yielded a virtual n = 2000 dataset for both baseline and induced cell death. From these data, an ROC curve was plotted and the AUROC and SEM calculated (GraphPad Prism 8). An example time series model can be found in Figure 1.

A similar methodology was utilized to test the influence of variations in post-treatment imaging time on the AUROC. Apoptosis initiation times were modeled as a Landau distribution as indicated above. Then, 2000 imaging start times were selected from either a Gaussian distribution (mean 48 hours, SD 24), a heavy tailed Landau distribution (mean 48

hours, sigma = 1), or a random (uniform) distribution. Time courses and numerical integration were then conducted for these data points as above.

Results

Using the literature search heuristic described in Figure 1, we analyzed previous studies of *in vivo* tumor apoptosis where tumor apoptosis as a function of post-treatment time was explicitly measured by *ex vivo* histopathology or immunohistochemical analysis (cell morphology, cleaved caspase 3, or TUNEL). From this we extracted the shape of the apoptosis-versus-time curve for each study as well as the full width at half maximum (FWHM), the time to maximum apoptotic response (treatment is initiated at t = 0), the maximum fold-change of apoptotic response over background (untreated tumor), and the standard deviation of the maximum response (SD). No obvious correlation between treatment type and the time-course of apoptotic response was observed. As seen in Table 1, the majority of the apoptosis time curves were unimodal (15/29, 52%) with a median post-treatment time-to-maximum of 24 hours. The median fold-change over non-treated tumors was 2.87. A minority of curves were bi-modal (4/29, 14%) or monotonic (10/29, 34%). For the purposes of subsequent simulations, only the unimodal model was considered. Graphical representations of the apoptosis time curves are provided in Figure 2. All of the extracted curves can be found in Supplementary Figure 1.

Formation of Induction Models:

A mathematical model of tumor apoptosis was constructed to understand the effect of sampling (integration) time on the expected imaging contrast ratio. However, since apoptosis may not be a phase-locked process, the initiation time of apoptosis could be intrinsically uncertain and was therefore considered a variable in the simulation. The underlying *distribution of the initiation of cell death* was simulated with a truncated Gaussian, Gaussian, truncated Landau, Landau, or uniform distribution. This is not to be confused with the *shape of the cell death function itself* which was confined to a Gaussian (unimodal) distribution. To prevent the initiation of apoptosis prior to day 0, the truncated Gaussian and Landau distributions were utilized such that the peak of induction would occur at 24 hr, the median time-to-maximum for unimodal responses (see Table 1). In this model, the probability of cell death induction prior to the start of treatment was set to 0. For the non-truncated Gaussian and Landau distributions, peak apoptosis was set at 48 hr which minimizes initiation prior to time 0. We note that while 48 hour initiation was not the median initiation time, it was represented within the *ex vivo* data sets. Integration times were varied between 30 minutes and 216 hours.

The Gaussian Induction Model:

As seen in Figure 3, for very well controlled initiation of cell death, a diagnostic ROC can be achieved with integration times < 1 hr which is consistent with typical PET radiotracers. Indeed, contrast ratios approaching 2 were observed with diagnostically acceptable AUROC > 0.9 depending upon the peak of apoptosis induction. However, these models demonstrated diminishing returns with integration time. Since Gaussian distributions truly converge to 0, and since the initiation times in this model were effectively known *a priori*, the AUROC for

longer integration times begins to decrease after reaching a peak at 50–75 hours. Once the probability of initiating cell death effectively reaches 0, integration covering these times only adds noise without adding any useful information or predictive power. Both Gaussian models reflect cases where the induction of cell death shows low variability and the time to maximal induction is known with high confidence.

The Landau Induction Model:

A second model of tumor apoptosis was constructed where the initiation of tumor apoptosis was simulated by a Landau distribution. This is effectively a "long-tailed" asymmetric Gaussian distribution centered around 48 hours post-treatment and represented moderate levels of uncertainty regarding the initiation of tumor cell death (Figure 4). A truncated Landau distribution centered at 24 hours post-treatment was also used. In these models, contrast ratios approaching 2 could be obtained with relatively short integration times (contrast ratio = 1.9 with a 3 hour integration time). However, predictive power was significantly decreased relative to Gaussian induction models and longer integration times were required to yield an AUROC of > 0.8. Even at the longest integration times, significant variation in the simulated contrast ratios led to AUROC values that approached, but did not reach, unity. In contrast to the Gaussian models, minimal diminishing returns were found for the longest integration times.

The Uniform Induction Model:

To reflect very low levels of certainty regarding cell death initiation times, induction of apoptosis was simulated to occur randomly from 24 hours to 11 days post-treatment (Figure 5). Short integration times (30 minutes – 9 hours) in this model, yielded median contrast ratios of < 1.3 with poor predictive value (AUROC ~ 0.6). Median contrast ratios approaching 1.5 were only obtained for integration times longer than 216 hours. ROC analysis showed high predictive power for the 216 hour integrator (AUROC ~ 0.9).

Imaging Start Time Uncertainty:

In addition to simulating uncertainty in the initiation of tumor death, we sought to determine the effect of imaging start time uncertainty on the median contrast ratio in the Landau model. This uncertainty represented the variability of patient imaging time following the start of treatment and was simulated using Gaussian, Landau and uniform probability distributions centered at 48 hours post-treatment. When the cell death initiation time and imaging start time were allowed to vary, the diagnostic potential of even the longest integration time dramatically decreased from ~ 0.9 to ~ 0.7 (Figure 6). We still continued to observe a mild increase in the AUROCs with increasing integration time, but because the peak of apoptosis induction could be easily missed, adding additional integration time yielded substantially less predictive power than when the imaging start time was fixed and early. Notably, both the uniform and Landau distributions of imaging start time yield similar diagnostic power.

Discussion

We have examined the effects of several key timing variables on the final diagnostic value of hypothetical molecular imaging reporters for cell death. *In vivo*, the signal of any injectable reporter represents the convolution of two processes, with each process defined by multiple rate constants. The first process to consider is the activity of the imaging agent. This includes the local uptake and washout of the reporter, binding/association with the biological target, dissociation from the target, biological half-life (clearance), and the half-life of the reporter (radioactive isotope). The second process under consideration is the underlying time-dependent shape of the local target concentration. This is a combination of multiple rate constants including target synthesis, target degradation, target compartmentalization, and target inhibition. If the target is an enzyme, the time dependent k_{cat} and K_m as well as the local concentration of any required co-substrates or co-factors also becomes relevant to the analysis. Finally, the biological clearance rate of the associated target complex, either through inactivation or clearance by the immune system (apoptotic bodies), must be taken into account in order to define the effective concentration of target over time.

In order to parse this multi-variate problem we chose to model an ideal scenario. The model was fundamentally optimistic as it assumed that both wash-in and wash out were instantaneous (delta functions). In the case of a real reporter undergoing biological clearance and radioactive decay, wash-in and washout kinetics will yield a decrease in the underlying contrast ratio by broadening the response function over time, resulting in exponential weighting of earlier time points. To deal with the complexity of the underlying target concentration, descriptive models were utilized based upon a literature review of the shapes and timing of cell death (both apoptosis and necrosis) after a single insult. The most commonly described shape of the cell death response was either unimodal or monotonic (which could be the initiation of a variety of distributions). This shape was utilized for the underlying time course to be interrogated and the height and width were set by the median value of the contrast ratios and FWHM described in the literature. These descriptive models were varied in their initiation of apoptosis by including multiple different models of induction, and applying the same models to tracer injection times. Each was sampled with different integration times.

Each integration time could be mapped onto the fastest off-rate constant for a given reporter. For example, consider a long-circulating, high-affinity antibody (k_{off} measured in hours to days with a comparable systemic clearance rate). If this antibody were labeled with carbon-11 (half-life 20.3 min), it would fall within the short integration time regime. If it were labeled with a longer lived isotope such as zirconium-89 it would fall within the long integration time regime. Similarly, small molecules with short biological half-lives fall within the short integration time regime regardless of the conjugated radionuclide. Less intuitively, biological clearance of the bound target also effectively decreases the integration time. At some point during cell death caspases will lose their catalytic activity and membrane compromised cells will be cleared from the milieu by the immune system, effectively shortening the integration time. These rate constants would also be context dependent. For example the rate of clearance of apoptotic bodies from normal non-immune privileged sites is fast, but in immune privileged sites such as a tumor or the eye[41] rates

could be much slower. The convolution of rate constants for all of these processes and interactions defines the available imaging time window (integration time). We propose that short integration times, driven by rapid radionuclide decay, fast systemic clearance, or transient target availability would be particularly susceptible to timing variability in the initiation of apoptosis. Conversely, long integration times would more robustly sample the apoptotic landscape leading to higher contrast ratios and predictive power. If true, this presents a compelling argument for the use of long-circulating probes conjugated to long-lived radionuclides that target long-lived epitopes/activities within the microenvironment of the dying tumor.

Given the inherently small difference in apoptotic activity between treated and untreated tumors (< 2.9-fold, Table 1), we predicted that the integration time would have a significant effect on the predicted contrast ratio. The variability in the time until maximum apoptotic response in pre-clinical studies also suggested that long integration times would be critical to obtain acceptable contrast ratios in cases of timing uncertainty. When the onset of apoptosis was known with high certainty, as reflected in the Gaussian model, the predicted contrast ratio of the imaging procedure was nearly 100% of the theoretical contrast ratio for all integration times. However, when the initiation of tumor apoptosis was highly uncertain, as in the uniform model, the predicted contrast ratio and AUROC were linearly dependent on integrator times > 72 hours and effectively integrator time-independent at < 72 hours. Moreover, the predictive power of imaging as measured by AUROC never reached a clinically-relevant value for integration times < 200 hours. Although this model suggested a somewhat unreasonable level of uncertainty in the initiation of tumor cell death (between 1 and 8 days post-treatment), the model nevertheless illustrated how the combination of short imaging times and high biological uncertainty degraded image contrast and predictive power.

A more realistic depiction of the uncertainty in tumor apoptosis initiation was provided by the Landau model. In this model, most cases of tumor apoptosis occurred in the predicted time range, but a smaller number of cases occurred at much longer post-treatment times. Contrast ratio was still strongly dependent on integration time, but acceptable AUROC values were obtained with integration times less than 72 hours. This interrogation time could be obtainable using [89]Zr-conjugated antibodies or other agents with similarly long isotopic and biological half-lives. Short integration times in this model were predicted to result in reasonable, but not clinically actionable predictive values (AUROC ~ 0.75).

A survey of the PET/SPECT apoptosis imaging literature (Table 2) indicates that the Landau model appropriately simulated variability in the timing of apoptosis initiation. The extracted normalized data can be found in Supplementary Figure 2. Imaging time course data provided in these studies was strikingly similar to the *ex vivo* histopathology data shown in Table 1. When only the unimodal responses were considered, the median values of FWHM and time to maximum apoptotic response in rodents corresponded almost perfectly to those obtained by *ex vivo* analysis. In addition, the median fold-change at max (1.99) was very close to the predicted contrast ratio for the 3 hour integrator in the Landau model (1.9). When only [18]F- and ^{99m}Tc-based tracers are considered, the median contrast ratio in rodent models dropped to 1.8. In human studies where a unimodal response was observed, the fold-

change at max was slightly higher than in rodent models (3.7), while the FWHM was significantly reduced (14.1). Although this represented only a single data point, it suggests that the magnitude of the apoptotic response in a clinical setting may be higher than in pre-clinical rodent models although the duration of the response (FWHM) may be significantly shorter. When the more rapid onset of this response was considered (4 hours until max response versus 24 hours in rodents), a long integration time may still be essential to avoid missing the bulk of the apoptotic signal in human tumors. Given the paucity of apoptosis imaging data in human patients, we are reluctant to draw definitive conclusions regarding the optimal integration time from this sparse data set.

Our simulations indicated that addition of uncertainty in the start of the imaging procedure would dramatically reduce the contrast ratio and predictive power of nearly all PET/SPECT apoptosis imaging agents. Although this variable may be less relevant in pre-clinical imaging studies where imaging experiments are tightly controlled, it is likely to play a major role in clinical settings, particularly in the case of clinical trials. While PET operational data in the literature were scarce, a report by Beyer and colleagues showed a 3–7 day wait time between referral and imaging at 30% of PET imaging facilities. In 15% of sites, the post-referral wait time could exceed 8 days. Clinical imaging trial protocols often allow similar flexibility between treatment and imaging in order to maintain patient recruitment levels. Our models indicate that 24 h of imaging time variability would significantly degrade predictive power of apoptosis imaging to values far below the level where clinical decisions can be made.

Limitations of the models.

As enumerated earlier, this model represented an ideal imaging experiment. Multiple doses during the course of treatment, as is common with cancer therapeutics, could affect cell death dynamics and broaden response. Broadening the response would ultimately decrease the susceptibility of the shorter lived reporters to multiple variables but particularly, the uncertainty in the timing of the injection of the imaging agent. The onset of apoptosis would also be less important (but not fall to zero) depending on whether multiple treatments caused a spike followed by return to baseline, or increased the baseline level of tumor cell death (best case scenario). Unfortunately, there were very few examples of multiple intervention therapy associated with apoptosis time course studies in the literature. However, these would be exciting and highly informative studies and we look forward to incorporating the results into our models as more pre-clinical and clinical data become available. It is also worth considering that the value of apoptosis imaging diminishes as the course of therapy goes on and collapses to zero once anatomic imaging of tumor size is completed (RECIST). The primary benefit from cell death imaging is rapid evaluation of treatment efficacy which would be most beneficial if carried out early in the therapeutic course. The use of apoptosis imaging in the context of multiple therapeutic interventions would therefore have to be carefully considered to balance clinical information with patient risk.

As stated above, we have considered only a unimodal model of tumor apoptosis to predict the contrast ratio and predictive power of molecular imaging agents. As seen in Tables 1 and 2, there was evidence of both bimodal and monotonic apoptosis response curves in the

literature. It was not clear that any improvements in contrast ratio or predictive power would be observed in bimodal responses since the minor peak typically occurs soon after treatment (<4 h) and is significantly more narrow than the major peak. This could lead to underestimation of the total apoptotic response at early imaging time-points, particularly if imaging fell between the minor and major peaks.

The monotonic apoptotic responses comprise a large fraction of the time courses documented in the literature (~34%) and could be sub-categorized into exponential, hyperbolic, sigmoidal, and biphasic (Figure 2). It was unclear whether these curves represented the early part of a long-duration unimodal response that was not interrogated by the addition of later sampling times. If this were the case, these curves may represent a sufficiently low-frequency apoptotic process as to be amenable to apoptosis imaging with short integration times. Future modeling studies will be carried out to validate this hypothesis.

Finally, the number of papers here are clearly insufficient to discriminate the shape of the underlying distribution of apoptotic response. Initiation times and FWHM are also subject to sparse sampling of the underlying time course. To address this, we tested multiple distributions to identify common results that were robust to the underlying ground truth. When required, we utilized median rather than mean values to generate our models. The median was a descriptor of the central location that was less sensitive to changes in the shape of the underlying distribution particularly if the underlying distribution involved heavy tails and/or asymmetry. As additional cell death time course data become available, we anticipate further refinement of our models.

Implications for Molecular Imaging.

A unimodal, high-frequency model of tumor apoptosis was chosen to study the effect of image timing variability on image contrast and predictive power. For processes that were indeed truly well-controlled, the unimodal response appeared, at first glance, to be a sufficiently well-defined and predictable process for molecular imaging with short integration times. While this assumption may hold in pre-clinical mouse tumor models where the tumor is more homogeneous (grown from a clonal population), pharmacokinetic variability is constrained through the use of inbred strains, and imaging procedures could be scheduled precisely, it is likely to break down when these factors are no longer present. Indeed, our models suggested that significant time variability in the apoptotic response was likely to preclude the utility of short integration times, and by extension, fast clearing probes with short half-life radionuclides. Only in the case where there was minimal uncertainty in the initiation of tumor apoptosis were these probes predicted to yield sufficient contrast and predictive power for clinical use. Besides apoptosis and necrosis, there are many emerging forms of cell death all of which likely co-exist. If one of these biological systems consistently leads to long, broad induction with high target stability, then short-lived reporters might re-emerge with new targets of interest.

Because it will be rare to fully define the underlying distribution of both the initiation of cell death, and the shape of the cell death process, it is important to consider the integration times that were most robust to the underlying models. The results in this work suggested that

longer integration times relative to standard 18-fluorine and 11-carbon isotopes will be necessary for high contrast ratios when the timing of tumor apoptosis is uncertain. In the case of PET/SPECT, this implies that slow-clearing probes conjugated to long-lived radioisotopes have a greater chance of detecting tumor cell death with high predictive power (AUROC > 0.9). This is supported by promising pre-clinical data of radiolabeled anti-phosphatidylserine antibodies and longer circulating Annexin V analogues, although translation to the clinic has yet to be demonstrated[36, 49]. If the underlying process of necrosis is more stable or broader than apoptosis then this might also explain the potential utility of the PS class of reporters. The requisite longer-lived isotopes, however, will require a concomitant trade-off with unfavorable dosimetry profiles. In oncologic applications with a single imaging time point this may indeed be an acceptable safety trade off, but careful consideration is required for patient populations with better expected outcomes. This conclusion is also supported by the time course imaging data from bioluminescence imaging studies. As seen in Table 2, contrast ratios obtained from bioluminescence imaging in split luciferase systems (e.g. pcFluc-DEVD) showed significantly higher fold-change at max values than those obtained in nuclear imaging studies. In these systems, imaging signal is being continuously produced at the site of apoptosis and effectively provides days of integration time with no apoptosis-independent signal decay. Although these models are non-translatable, they do provide an existence proof of high contrast from long integration times of apoptotic reporters.

Supplementary Material

Refer to Web version on PubMed Central for supplementary material.

Acknowledgements

References

1. Levine B; Kroemer G, Autophagy in the pathogenesis of disease. Cell 2008, 132 (1), 27–42. [PubMed: 18191218]

2. Hotchkiss RS; Nicholson DW, Apoptosis and caspases regulate death and inflammation in sepsis. Nature reviews. Immunology 2006, 6 (11), 813–822.

3. Chen Q; Kang J; Fu C, The independence of and associations among apoptosis, autophagy, and necrosis. Signal Transduct Target Ther 2018, 3, 18. [PubMed: 29967689]

4. Kondo Y; Kanzawa T; Sawaya R; Kondo S, The role of autophagy in cancer development and response to therapy. Nat Rev Cancer 2005, 5 (9), 726–34. [PubMed: 16148885]

5. Litière S; Isaac G; Vries ED; Bogaerts J; Chen AP; Dancey J; Ford R; Gwyther SJ; Hoekstra OS; Huang E; Lin NU; Liu Y; Mandrekar SJ; Schwartz LH; Shankar L; Therasse P; Seymour L; Group RW, Validation of RECIST 1.1 for use with cytotoxic agents and targeted cancer agents (TCA): Results of a RECIST Working Group analysis of a 50 clinical trials pooled individual patient database. Journal of Clinical Oncology 2017, 35 (15_suppl), 2534–2534.

6. Bullok K; Piwnica-Worms D, Synthesis and characterization of a small, membrane-permeant, caspase-activatable far-red fluorescent peptide for imaging apoptosis. Journal of medicinal chemistry 2005, 48 (17), 5404–7. [PubMed: 16107137]

7. Engel BJ; Gammon ST; Chaudhari R; Lu Z; Pisaneschi F; Yang H; Ornelas A; Yan V; Kelderhouse L; Najjar AM; Tong WP; Zhang S; Piwnica-Worms D; Bast RC Jr.; Millward SW, Caspase-3 Substrates for Noninvasive Pharmacodynamic Imaging of Apoptosis by PET/CT. Bioconjugate chemistry 2018, 29 (9), 3180–3195. [PubMed: 30168713]

8. Xia CF; Chen G; Gangadharmath U; Gomez LF; Liang Q; Mu F; Mocharla VP; Su H; Szardenings AK; Walsh JC; Zhao T; Kolb HC, In vitro and in vivo evaluation of the caspase-3 substrate-based radiotracer [(18)F]-CP18 for PET imaging of apoptosis in tumors. Molecular imaging and biology : MIB : the official publication of the Academy of Molecular Imaging 2013, 15 (6), 748–57.

9. Nguyen QD; Lavdas I; Gubbins J; Smith G; Fortt R; Carroll LS; Graham MA; Aboagye EO, Temporal and spatial evolution of therapy-induced tumor apoptosis detected by caspase-3-selective molecular imaging. Clinical cancer research : an official journal of the American Association for Cancer Research 2013, 19 (14), 3914–24.

10. Zhou D; Chu W; Chen DL; Wang Q; Reichert DE; Rothfuss J; D'Avignon A; Welch MJ; Mach RH, [18F]- and [11C]-labeled N-benzyl-isatin sulfonamide analogues as PET tracers for apoptosis: synthesis, radiolabeling mechanism, and in vivo imaging study of apoptosis in Fas-treated mice using [11C]WC-98. Org Biomol Chem 2009, 7 (7), 1337–48. [PubMed: 19300818]

11. Elvas F; Stroobants S; Wyffels L, Phosphatidylethanolamine targeting for cell death imaging in early treatment response evaluation and disease diagnosis. Apoptosis 2017, 22 (8), 971–987. [PubMed: 28623512]

12. Neves AA; Xie B; Fawcett S; Alam IS; Witney TH; de Backer MM; Summers J; Hughes W; McGuire S; Soloviev D; Miller J; Howat WJ; Hu DE; Rodrigues TB; Lewis DY; Brindle KM, Rapid Imaging of Tumor Cell Death In Vivo Using the C2A Domain of Synaptotagmin-I. Journal of nuclear medicine : official publication, Society of Nuclear Medicine 2017, 58 (6), 881–887.

13. Wuest M; Perreault A; Kapty J; Richter S; Foerster C; Bergman C; Way J; Mercer J; Wuest F, Radiopharmacological evaluation of 18F-labeled phosphatidylserine-binding peptides for molecular imaging of apoptosis. Nuclear medicine and biology 2015, 42 (11), 864–874. [PubMed: 26205076]

14. Bauwens M; De Saint-Hubert M; Devos E; Deckers N; Reutelingsperger C; Mortelmans L; Himmelreich U; Mottaghy FM; Verbruggen A, Site-specific 68Ga-labeled Annexin A5 as a PET imaging agent for apoptosis. Nuclear medicine and biology 2011, 38 (3), 381–92. [PubMed: 21492787]

15. Laforest R; Dehdashti F; Liu Y; Frye J; Frye S; Luehmann H; Sultan D; Shan JS; Freimark BD; Siegel BA, First-in-Man Evaluation of (124)I-PGN650: A PET Tracer for Detecting Phosphatidylserine as a Biomarker of the Solid Tumor Microenvironment. Mol Imaging 2017, 16, 1536012117733349.

16. Smith BA; Gammon ST; Xiao S; Wang W; Chapman S; McDermott R; Suckow MA; Johnson JR; Piwnica-Worms D; Gokel GW; Smith BD; Leevy WM, In vivo optical imaging of acute cell death using a near-infrared fluorescent zinc-dipicolylamine probe. Mol Pharm 2011, 8 (2), 583–90. [PubMed: 21323375]

17. Belhocine TZ; Blankenberg FG; Kartachova MS; Stitt LW; Vanderheyden JL; Hoebers FJ; Van de Wiele C, (99m)Tc-Annexin A5 quantification of apoptotic tumor response: a systematic review and meta-analysis of clinical imaging trials. European journal of nuclear medicine and molecular imaging 2015, 42 (13), 2083–97. [PubMed: 26275392]

18. Dubash SR; Merchant S; Heinzmann K; Mauri F; Lavdas I; Inglese M; Kozlowski K; Rama N; Masrour N; Steel JF; Thornton A; Lim AK; Lewanski C; Cleator S; Coombes RC; Kenny L; Aboagye EO, Clinical translation of [(18)F]ICMT-11 for measuring chemotherapy-induced caspase 3/7 activation in breast and lung cancer. European journal of nuclear medicine and molecular imaging 2018, 45 (13), 2285–2299. [PubMed: 30259091]

19. Challapalli A; Kenny LM; Hallett WA; Kozlowski K; Tomasi G; Gudi M; Al-Nahhas A; Coombes RC; Aboagye EO, 18F-ICMT-11, a caspase-3-specific PET tracer for apoptosis: biodistribution and radiation dosimetry. Journal of nuclear medicine : official publication, Society of Nuclear Medicine 2013, 54 (9), 1551–6.

20. Meyn RE; Stephens LC; Ang KK; Hunter NR; Brock WA; Milas L; Peters LJ, Heterogeneity in the Development of Apoptosis in Irradiated Murine Tumours of Different Histologies. International Journal of Radiation Biology 1993, 64 (5), 583–591. [PubMed: 7902398]

21. Rupnow BA; Murtha AD; Alarcon RM; Giaccia AJ; Knox SJ, Direct Evidence That Apoptosis Enhances Tumor Responses to Fractionated Radiotherapy. Cancer research 1998, 58 (9), 1779–1784. [PubMed: 9581811]

22. Takei T; Kuge Y; Zhao S; Sato M; Strauss HW; Blankenberg FG; Tait JF; Tamaki N, Time Course of Apoptotic Tumor Response After a Single Dose of Chemotherapy: Comparison with 99mTc-Annexin V Uptake and Histologic Findings in an Experimental Model. Journal of Nuclear Medicine 2004, 45 (12), 2083–2087. [PubMed: 15585485]

23. Gerlinger M; Rowan AJ; Horswell S; Math M; Larkin J; Endesfelder D; Gronroos E; Martinez P; Matthews N; Stewart A; Tarpey P; Varela I; Phillimore B; Begum S; McDonald NQ; Butler A; Jones D; Raine K; Latimer C; Santos CR; Nohadani M; Eklund AC; Spencer-Dene B; Clark G; Pickering L; Stamp G; Gore M; Szallasi Z; Downward J; Futreal PA; Swanton C, Intratumor heterogeneity and branched evolution revealed by multiregion sequencing. N Engl J Med 2012, 366 (10), 883–892. [PubMed: 22397650]

24. Meyn RE; Stephens LC; Hunter NR; Milas L, Induction of apoptosis in murine tumors by cyclophosphamide. Cancer Chemotherapy and Pharmacology 1994, 33 (5), 410–414. [PubMed: 8306415]

25. Hozo SP; Djulbegovic B; Hozo I, Estimating the mean and variance from the median, range, and the size of a sample. BMC Medical Research Methodology 2005, 5 (1), 13. [PubMed: 15840177]

26. Higgens JPT, Green S, Cochrane Handbook for Systematic Reviews of Interventions. Version 5.1.0 ed.; The Cochrane Collaboration: 2011.

27. Takei T; Kuge Y; Zhao S; Sato M; Strauss HW; Blankenberg FG; Tait JF; Tamaki N, Time course of apoptotic tumor response after a single dose of chemotherapy: comparison with 99mTc-annexin V uptake and histologic findings in an experimental model. Journal of nuclear medicine : official publication, Society of Nuclear Medicine 2004, 45 (12), 2083–7.

28. Ljungkvist AS; Bussink J; Kaanders JH; Wiedenmann NE; Vlasman R; van der Kogel AJ, Dynamics of hypoxia, proliferation and apoptosis after irradiation in a murine tumor model. Radiat Res 2006, 165 (3), 326–36. [PubMed: 16494521]

29. Hickson J; Ackler S; Klaubert D; Bouska J; Ellis P; Foster K; Oleksijew A; Rodriguez L; Schlessinger S; Wang B; Frost D, Noninvasive molecular imaging of apoptosis in vivo using a modified firefly luciferase substrate, Z-DEVD-aminoluciferin. Cell death and differentiation 2010, 17 (6), 1003–10. [PubMed: 20057500]

30. Erba PA; Manfredi C; Lazzeri E; Minichilli F; Pauwels EK; Sbrana A; Strauss HW; Mariani G, Time course of Paclitaxel-induced apoptosis in an experimental model of virus-induced breast cancer. Journal of nuclear medicine : official publication, Society of Nuclear Medicine 2010, 51 (5), 775–81.

31. Vangestel C; Van de Wiele C; Mees G; Mertens K; Staelens S; Reutelingsperger C; Pauwels P; Van Damme N; Peeters M, Single-photon emission computed tomographic imaging of the early time course of therapy-induced cell death using technetium 99m tricarbonyl His-annexin A5 in a colorectal cancer xenograft model. Mol Imaging 2012, 11 (2), 135–47. [PubMed: 22469241]

32. Aide N; Poulain L; Briand M; Dutoit S; Allouche S; Labiche A; Ngo-Van Do A; Nataf V; Batalla A; Gauduchon P; Talbot JN; Montravers F, Early evaluation of the effects of chemotherapy with longitudinal FDG small-animal PET in human testicular cancer xenografts: early flare response does not reflect refractory disease. European journal of nuclear medicine and molecular imaging 2009, 36 (3), 396–405. [PubMed: 19050878]

33. Papaevangelou E; Almeida GS; Jamin Y; Robinson SP; deSouza NM, Diffusion-weighted MRI for imaging cell death after cytotoxic or apoptosis-inducing therapy. Br J Cancer 2015, 112 (9), 1471–9. [PubMed: 25880014]

34. Meyn RE; Stephens LC; Hunter NR; Milas L, Kinetics of cisplatin-induced apoptosis in murine mammary and ovarian adenocarcinomas. International journal of cancer. Journal international du cancer 1995, 60 (5), 725–9. [PubMed: 7860148]

35. Symmans WF; Volm MD; Shapiro RL; Perkins AB; Kim AY; Demaria S; Yee HT; McMullen H; Oratz R; Klein P; Formenti SC; Muggia F, Paclitaxel-induced apoptosis and mitotic arrest assessed by serial fine-needle aspiration: implications for early prediction of breast cancer response to neoadjuvant treatment. Clinical cancer research : an official journal of the American Association for Cancer Research 2000, 6 (12), 4610–7. [PubMed: 11156210]

36. Ke S; Wen X; Wu QP; Wallace S; Charnsangavej C; Stachowiak AM; Stephens CL; Abbruzzese JL; Podoloff DA; Li C, Imaging taxane-induced tumor apoptosis using PEGylated, 111In-labeled annexin V. Journal of nuclear medicine : official publication, Society of Nuclear Medicine 2004, 45 (1), 108–15.

37. Witham TF; Okada H; Fellows W; Hamilton RL; Flickinger JC; Chambers WH; Pollack IF; Watkins SC; Kondziolka D, The characterization of tumor apoptosis after experimental radiosurgery. Stereotact Funct Neurosurg 2005, 83 (1), 17–24. [PubMed: 15775705]

38. Wang F; Fang W; Zhao M; Wang Z; Ji S; Li Y; Zheng Y, Imaging paclitaxel (chemotherapy)-induced tumor apoptosis with 99mTc C2A, a domain of synaptotagmin I: a preliminary study. Nuclear medicine and biology 2008, 35 (3), 359–64. [PubMed: 18355692]

39. McAuliffe JC; Hunt KK; Lazar AJ; Choi H; Qiao W; Thall P; Pollock RE; Benjamin RS; Trent JC, A randomized, phase II study of preoperative plus postoperative imatinib in GIST: evidence of rapid radiographic response and temporal induction of tumor cell apoptosis. Ann Surg Oncol 2009, 16 (4), 910–9. [PubMed: 18953611]

40. Zheng YM; Wang F; Fang W; Hua ZC; Wang ZZ; Meng QL; Yan J, A preliminary study of imaging paclitaxel-induced tumor apoptosis with (99)Tc(m)-His10-Annexin V. Chin Med J (Engl) 2013, 126 (15), 2928–33. [PubMed: 23924470]

41. Qiu X; Johnson JR; Wilson BS; Gammon ST; Piwnica-Worms D; Barnett EM, Single-cell resolution imaging of retinal ganglion cell apoptosis in vivo using a cell-penetrating caspase-activatable peptide probe. PLoS One 2014, 9 (2), e88855.

42. Hu S; Kiesewetter DO; Zhu L; Guo N; Gao H; Liu G; Hida N; Lang L; Niu G; Chen X, Longitudinal PET imaging of doxorubicin-induced cell death with 18F-Annexin V. Molecular imaging and biology : MIB : the official publication of the Academy of Molecular Imaging 2012, 14 (6), 762–70.

43. Belhocine T; Steinmetz N; Hustinx R; Bartsch P; Jerusalem G; Seidel L; Rigo P; Green A, Increased uptake of the apoptosis-imaging agent (99m)Tc recombinant human Annexin V in human tumors after one course of chemotherapy as a predictor of tumor response and patient prognosis. Clinical cancer research : an official journal of the American Association for Cancer Research 2002, 8 (9), 2766–74. [PubMed: 12231515]

44. Mandl SJ; Mari C; Edinger M; Negrin RS; Tait JF; Contag CH; Blankenberg FG, Multi-modality imaging identifies key times for annexin V imaging as an early predictor of therapeutic outcome. Mol Imaging 2004, 3 (1), 1–8. [PubMed: 15142407]

45. Spaepen K; Stroobants S; Dupont P; Bormans G; Balzarini J; Verhoef G; Mortelmans L; Vandenberghe P; De Wolf-Peeters C, [(18)F]FDG PET monitoring of tumour response to chemotherapy: does [(18)F]FDG uptake correlate with the viable tumour cell fraction? European journal of nuclear medicine and molecular imaging 2003, 30 (5), 682–8. [PubMed: 12601498]

46. Niu G; Zhu L; Ho DN; Zhang F; Gao H; Quan Q; Hida N; Ozawa T; Liu G; Chen X, Longitudinal bioluminescence imaging of the dynamics of Doxorubicin induced apoptosis. Theranostics 2013, 3 (3), 190–200. [PubMed: 23471295]

47. Weber TG; Osl F; Renner A; Poschinger T; Galban S; Rehemtulla A; Scheuer W, Apoptosis imaging for monitoring DR5 antibody accumulation and pharmacodynamics in brain tumors noninvasively. Cancer research 2014, 74 (7), 1913–23. [PubMed: 24509903]

48. Scabini M; Stellari F; Cappella P; Rizzitano S; Texido G; Pesenti E, In vivo imaging of early stage apoptosis by measuring real-time caspase-3/7 activation. Apoptosis 2011, 16 (2), 198–207. [PubMed: 21082356]

49. Belzile O; Huang X; Gong J; Carlson J; Schroit AJ; Brekken RA; Freimark BD, Antibody targeting of phosphatidylserine for the detection and immunotherapy of cancer. Immunotargets Ther 2018, 7, 1–14. [PubMed: 29417044]

Example of tumor apoptosis induced with a peak 2 days post therapy that was imaged starting at day 1 and integrated for 48 hrs.
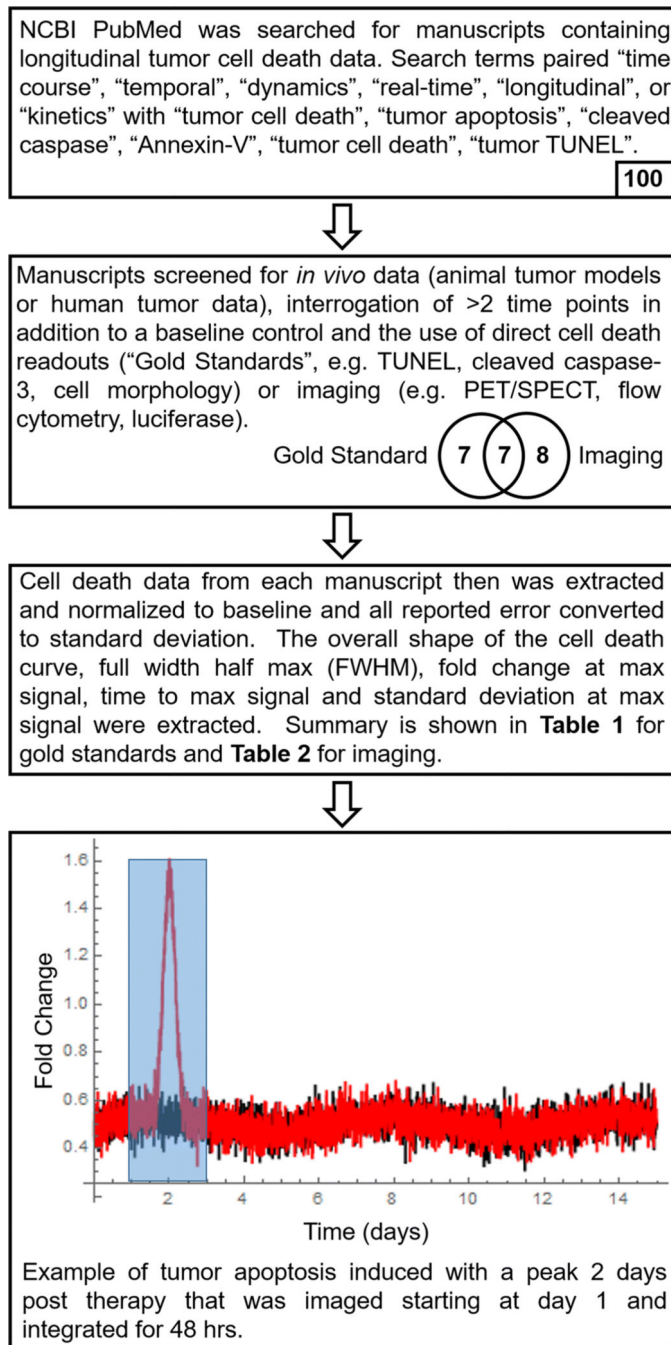
Figure 1: Extraction of Tumor Apoptosis Time Course Data from the Literature.
The tumor apoptosis literature was surveyed and filtered according to the criteria described in the top two boxes to obtain time-series data relating the amplitude of tumor apoptosis to the time post-treatment. The number at the bottom of each box indicates the number of manuscripts that met the stated criteria. The resulting time series data (Table 1) were used to construct a mathematical model of tumor apoptosis (red line) and background apoptosis (black line). This model was computationally integrated (e.g. shaded blue box) to obtain theoretical contrast ratios.
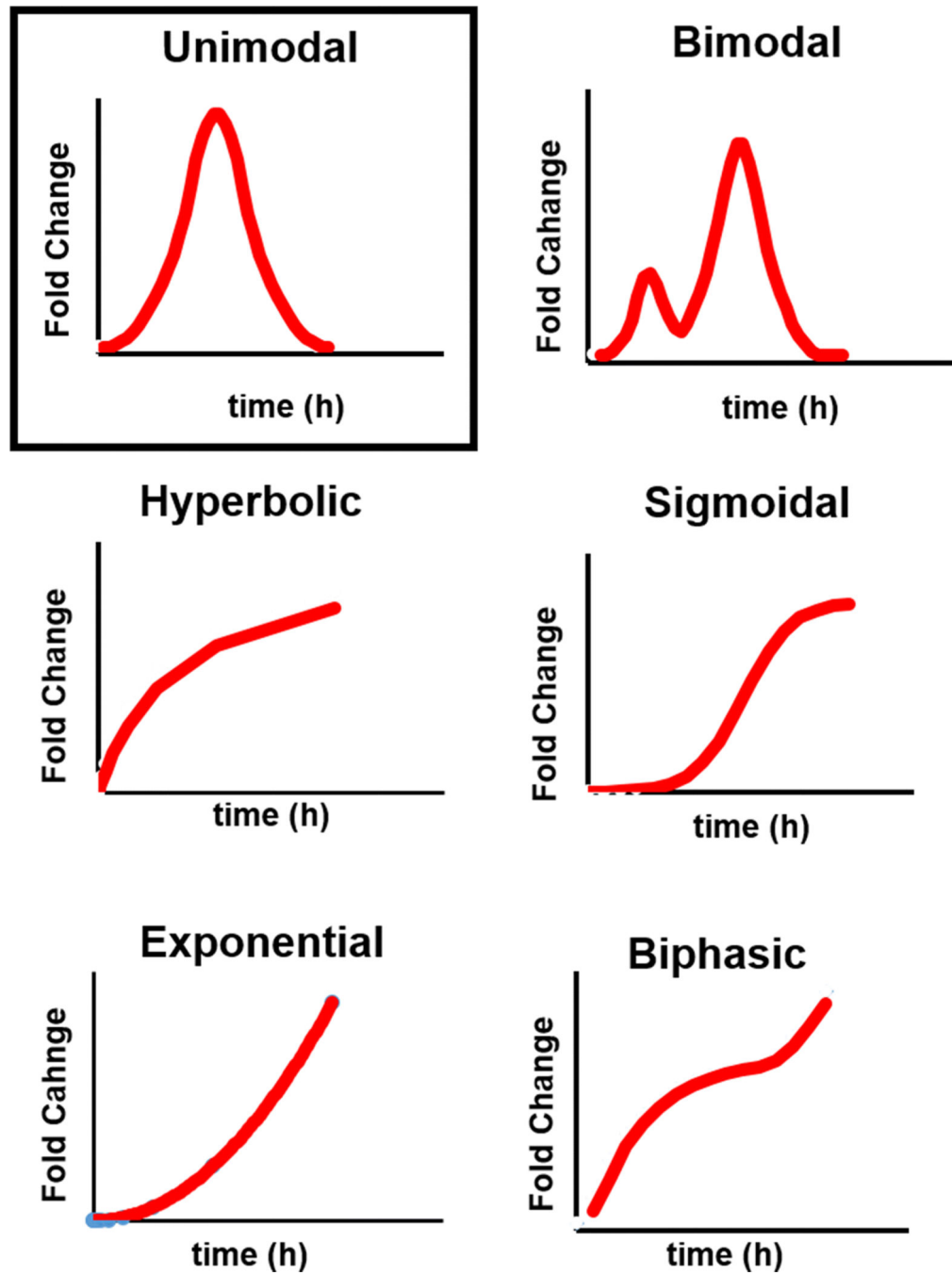
Figure 2: Apoptosis Time Curves Observed in the Literature.
Only unimodal curves (boxed) were considered in subsequent analyses.
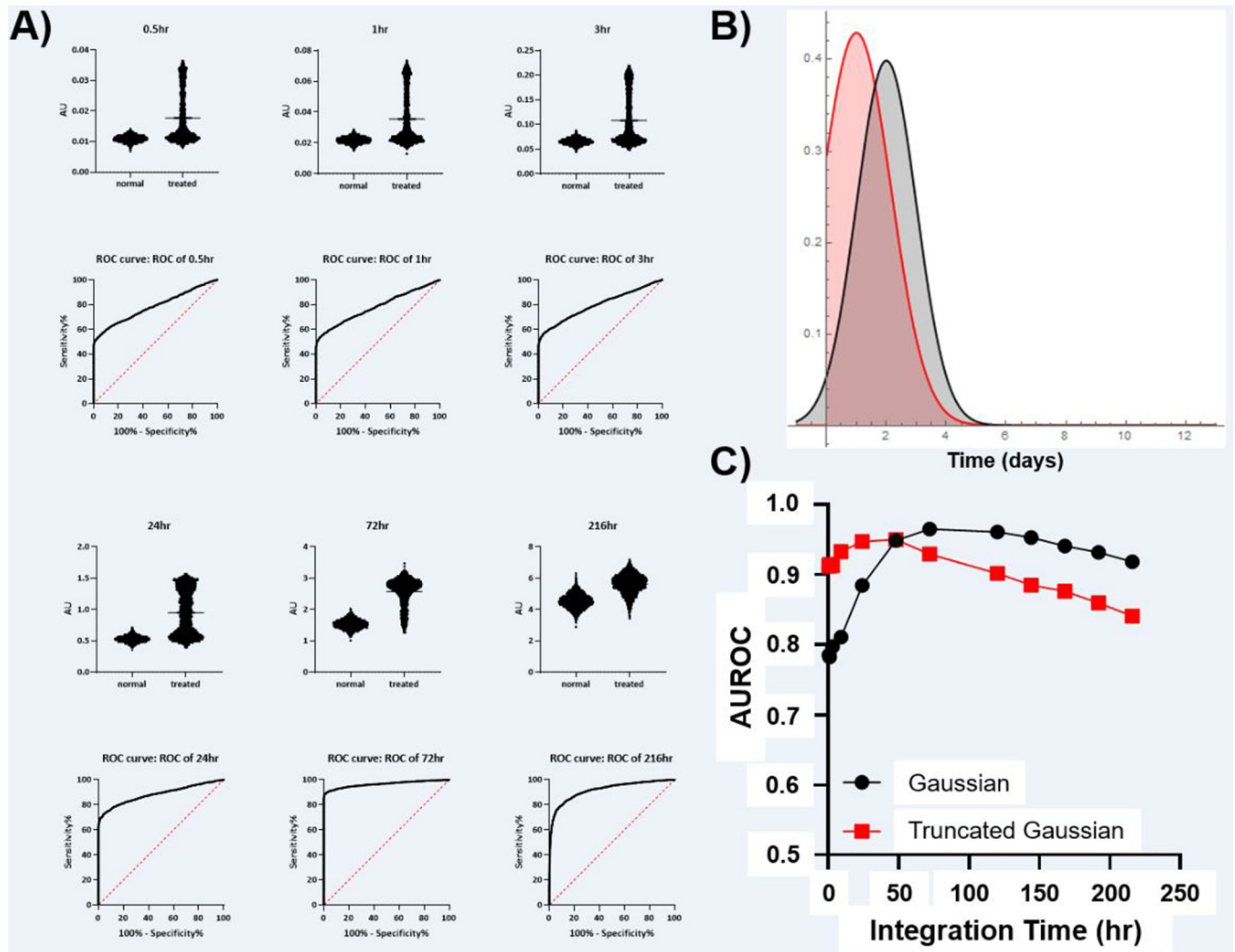
Figure 3: Simulation of Tumor Apoptosis with Gaussian and Truncated Gaussian Distributions of Apoptosis Initiation Time.

A) Simulated signal (AU) obtained with the imaging integration time shown at the top of each graph. The calculated ROC for each imaging integration time is shown below. **B)** The distribution of apoptosis induction times utilized in the experiments (red = truncated Gaussian, black = Gaussian. **C)** The relationship between integration time and AUROC for both Gaussian models of apoptosis start time (SEM is below the size of data points).
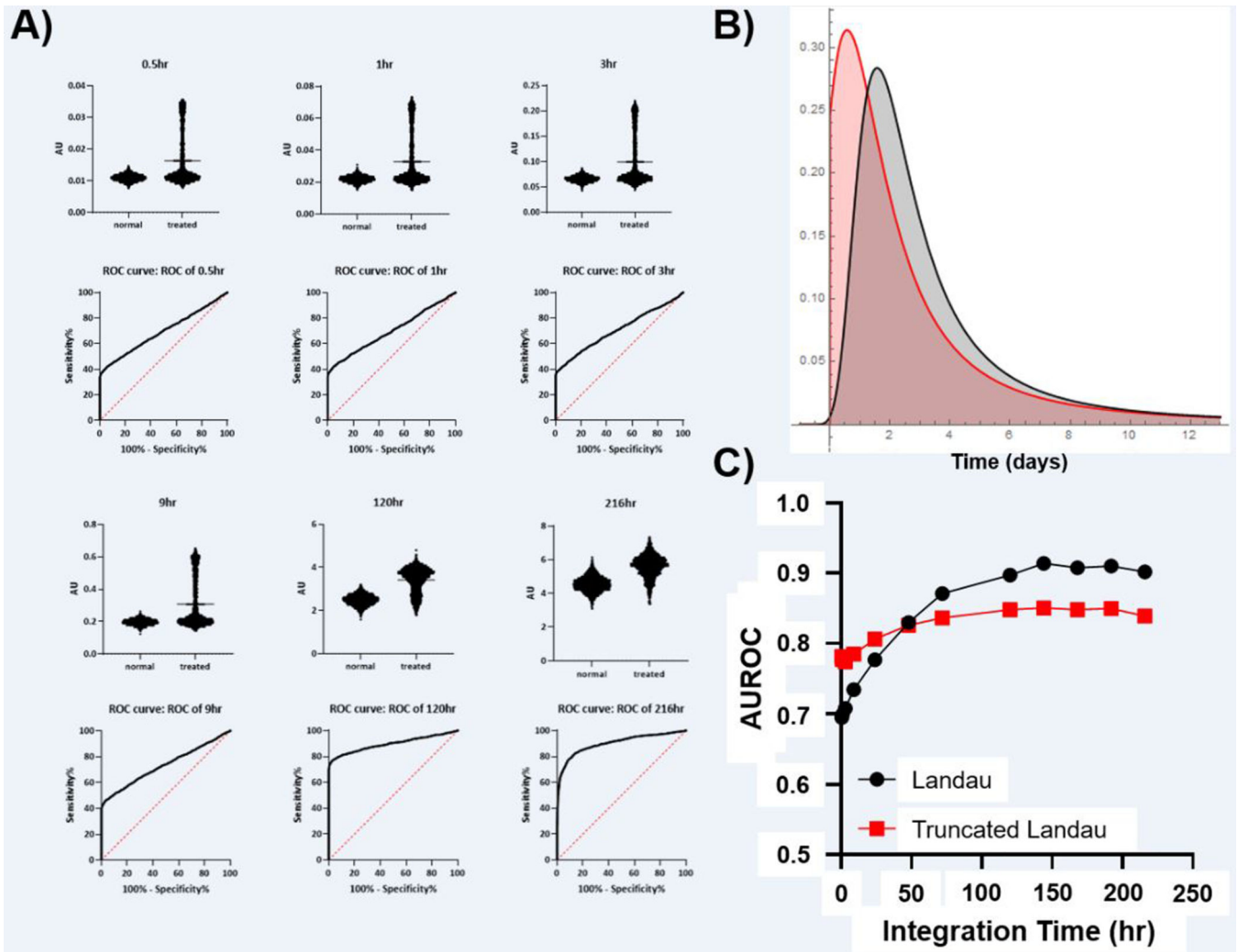
Figure 4: Simulation of Tumor Cell Death with Landau and Truncated Landau Distributions of Apoptosis Initiation Time.
A) Simulated signal (AU) obtained with the imaging integration time shown at the top of each graph. The calculated ROC for each imaging integration time is shown below. **B)** The distribution of apoptosis induction times utilized in the experiments (red = truncated Landau, black = Landau. **C)** The relationship between integration time and AUROC for both Landau models of apoptosis start time (SEM is below the size of data points).
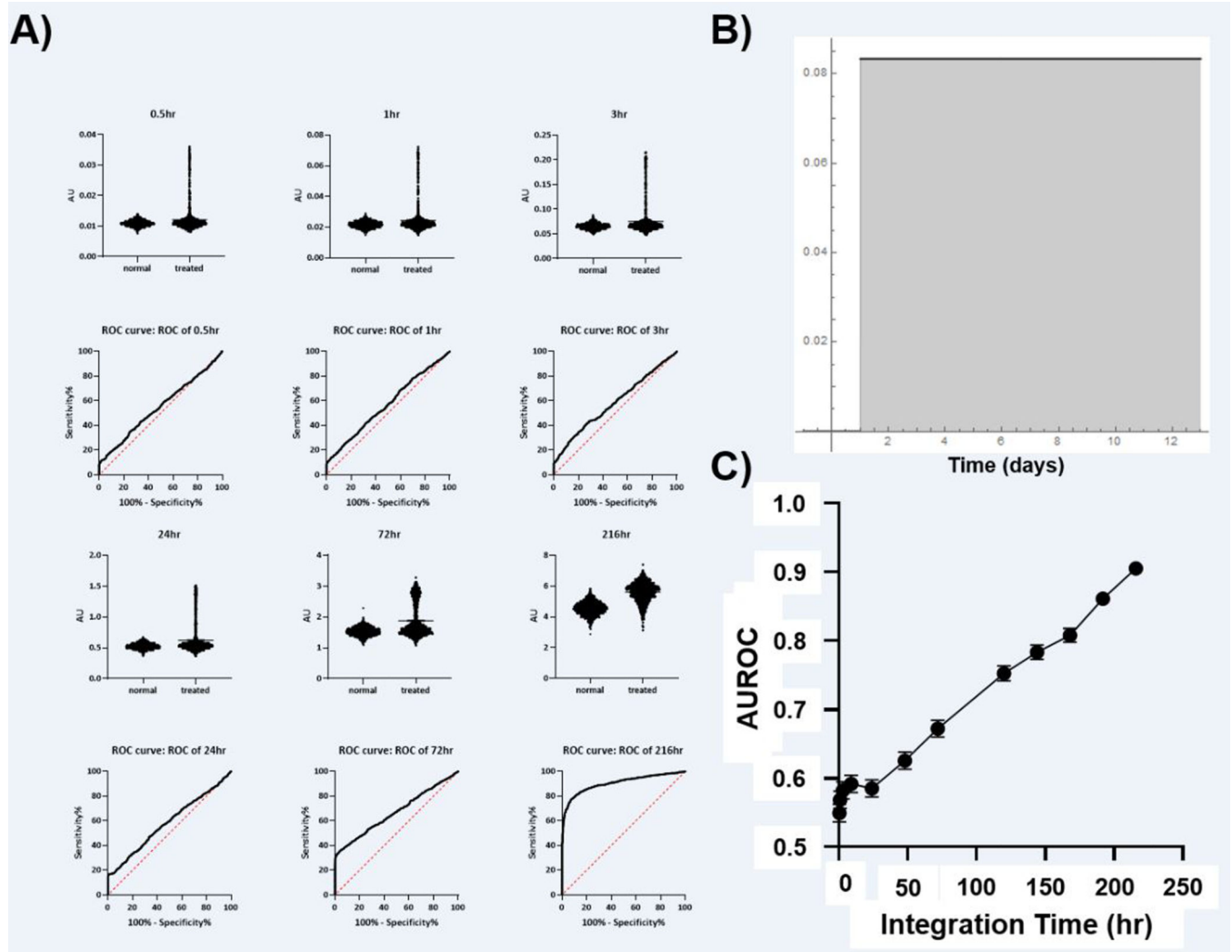
Figure 5: Simulation of Tumor Cell Death with a Uniform Distribution of Apoptosis Initiation.
A) Simulated signal (AU) obtained with the imaging integration time shown at the top of each graph. The calculated ROC for each imaging integration time is shown below. **B)** The distribution of apoptosis induction times utilized in the experiments. **C)** The relationship between integration time and AUROC for the uniform model of apoptosis start time (error bars show the SEM).

Figure 6. Variable Imaging Start Time Reduces Predictive Power.
If a subject is imaged later than the peak induction of cell death, the diagnostic potential dramatically decreases. While longer integration time does capture the longer tails of the induced apoptosis, a fixed early imaging time is critical to enable AUROC > 0.85.

Table 1:

Summary of Apoptosis Time Course Data Obtained from the Literature.

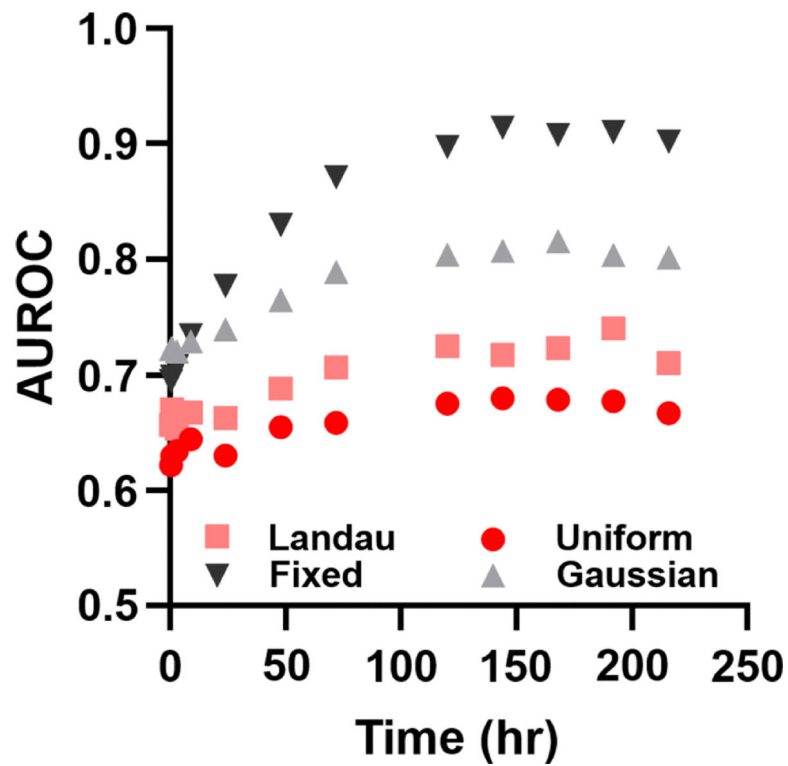| Reference	Treatment	Model	Detection Method	Curve Type	FWHM (h)	Time to Max (h)	Fold Change at Max	SD at Max (%)
27	Cyclophosphamide	Rats	Cleaved cas-3	Monotonic	N/A	20	2.11	35.4
28	Radiation (overall)	Mice	Cleaved cas-3	Unimodal	13.8	4	2.98	54.7
28	Radiation (initially hypoxic)	Mice	Cleaved cas-3	Unimodal	15.9	8	2.57	37.5
28	Radiation (initially normoxic)	Mice	Cleaved cas-3	Unimodal	14.5	4	9.85	48.4
29	Docetaxel	Mice	Cleaved cas-3	Monotonic	N/A	72	4.19	35.1
30	Paclitaxel	Mice	Cleaved cas-3	Bimodal	1.5, 14	6	2.86	39.9
31	Irinotecan	Mice	Cleaved cas-3	Bimodal	3.5, >30.1	24	3.23	17.6
31	5-FU	Mice	Cleaved cas-3	Unimodal	16.1	8	1.86	7.9
32	Cisplatin	Rats	Cleaved cas-3	Monotonic	N/A	96	23.8	64.7
31	Bevacizumab	Mice	Cleaved cas-3	Unimodal	14.2	24	2.05	7.9
31	Oxaliplatin	Mice	Cleaved cas-3	Unimodal	26.9	24	3.89	3.5
31	Panitumumab	Mice	Cleaved cas-3	Bimodal	3.1, 7.9	4	1.67	25.1
33	Birinapant	Mice	Cleaved cas-3	Unimodal	>77	72	2.87	14
33	Irinotecan	Mice	Cleaved cas-3	Monotonic	N/A	120	3.7	21.2
34	Cisplatin	Mice	Morphology	Unimodal	23.2	18	4.58	NR
34	Cisplatin	Mice	Morphology	Bimodal	52.4	18	8	NR
35	Paclitaxel (no response)	Human	Morphology	Unimodal	31.5	24	2.08	65.5
35	Paclitaxel (partial response)	Human	Morphology	Unimodal	51.1	72	4.48	25.7
35	Paclitaxel (complete response)	Human	Morphology	Monotonic	N/A	72	3.98	23.5
36	C225	Mice	Morphology	Unimodal	60.8	24	1.63	16.8
36	Paclitaxel	Mice	Morphology	Monotonic	N/A	96	4.55	9.5
27	Cyclophosphamide	Rats	TUNEL	Monotonic	N/A	20	1.8	19.3
37	Radiation	Rats	TUNEL	Unimodal	59.2	48	2.07	11.6
38	Paclitaxel	Mice	TUNEL	Monotonic	N/A	72	28.34	12.5
39	Imatinib	Human	TUNEL	Monotonic	N/A	168	7.5	NR
30	Paclitaxel	Mice	TUNEL	Unimodal	2.9	3	6.91	70.3
40	Paclitaxel	Mice	TUNEL	Monotonic	N/A	72	25.61	11.7
33	Birinapant	Mice	TUNEL	Unimodal	89.5	72	2.18	27
33	Irinotecan	Mice	TUNEL	Unimodal	80.5	72	2.88	10.2
Median (Unimodal Responses) Overall					**26.9**	**24**	**2.87**	
Median (Unimodal Responses) Human					**41.3**	**48**	**3.28**	
Median (Unimodal Responses) Rodent					**19.6**	**24**	**2.87**	

NR = not reported. Two FWHM values are provided for the bimodal data.

Table 2:

Summary of Apoptosis Time Course Data Obtained from Imaging Experiments.

Reference	Treatment	Model	Radiotracer	Curve Type	FWHM (h)	Time to Max (h)	Fold Change at Max	SD at Max (%)
9	Cyclophosphamide	Mice	[^{18}F]F-ICMT-11	Unimodal	>36	24	1.99	36.9
9	Birinapant	Mice	[^{18}F]F-ICMT-11	Unimodal	15	6	1.54	42.7
42	Doxorubicin	Mice	[^{18}F]F-Annexin V	Unimodal	97	72	1.76	6.9
36	Paclitaxel	Mice	[^{111}In]In-DTPA-PEG-Annexin V	Monotonic	N/A	96	1.75	12.8
36	C225	Mice	[^{111}In]In-DTPA-PEG-Annexin V	Unimodal	24.8	24	1.14	21.3
31	5-FU	Mice	[^{99m}Tc]Tc-(CO)$_3$-His-Annexin A5	Bimodal	25.4	8	1.52	9.1
31	Irinotecan	Mice	[^{99m}Tc]Tc-(CO)$_3$-His-Annexin A5	Unimodal	24.4	24	1.56	1.3
31	Oxaliplatin	Mice	[^{99m}Tc]Tc-(CO)$_3$-His-Annexin A5	Unimodal	27.7	24	1.79	7.6
31	Bevacizumab	Mice	[^{99m}Tc]Tc-(CO)$_3$-His-Annexin A5	No increase	3.7	24	1.07	14.1
31	Panitumumab	Mice	[^{99m}Tc]Tc-(CO)$_3$-His-Annexin A5	Bimodal	3.2, 16	24	1.62	6.9
43	Mitomyci, Ifosfamide, cis-Platinum	Human	[^{99m}Tc]Tc-BTAP-Annexin V	Monotonic	N/A	24	4.3	94.5
43	Adriamycin, Bleomycin, Vincristine, Doxorubicin	Human	[^{99m}Tc]Tc-BTAP-Annexin V	Monotonic	N/A	24	2.9	0
43	Cyclophosphamide, Doxorubicin, Vincristine, Prednisone	Human	[^{99m}Tc]Tc-BTAP-Annexin V	Monotonic	N/A	24	3.2	0
43	Etoposide	Human	[^{99m}Tc]Tc-BTAP-Annexin V	Unimodal	14.1	4	3.7	0
44	Doxorubicin	Mice	[^{99m}Tc]Tc-Annexin V-117	Bimodal	1.5, 27.9	12	2.07	19.7
38	Paclitaxel	Mice	[^{99m}Tc]Tc-C2A-GST	Monotonic	N/A	72	3.27	43.4
40	Paclitaxel	Mice	[^{99m}Tc]Tc-His$_{10}$-Annexin V	Monotonic	N/A	72	3.09	28.2
27	Cyclophosphamide	Rats	[^{99m}Tc]Tc-HYNIC-Annexin V	Monotonic	N/A	20	1.56	9.1
30	Paclitaxel	Mice	[^{99m}Tc]Tc-HYNIC-Annexin V	Unimodal	3.5	3	1.79	0.6
45	Cyclophosphamide	Mice	Annexin-V FC	Unimodal	85.8	24	1.35	26.8
38	Paclitaxel	Mice	Cleaved caspase-3 FC	Monotonic	N/A	72	35.64	6.7
40	Paclitaxel	Mice	Cleaved caspase-3 FC	Monotonic	N/A	72	22.56	12.2
46	Doxorubicin (1st dose)	Mice	pcFluc-DEVD	Unimodal	342.9	264	23.1	34.2
46	Doxorubicin (2nd dose)	Mice	pcFluc-DEVD	Unimodal	178.7	264	31.6	26.9
47	anti–DR5-Cy5 antibody (1st dose)	Mice	pcFluc-DEVD	Unimodal	6	4	19.5	54.8
47	anti–DR5-Cy5 antibody (2nd dose)	Mice	pcFluc-DEVD	Unimodal	5.6	4	5.88	178.8

Reference	Treatment	Model	Radiotracer	Curve Type	FWHM (h)	Time to Max (h)	Fold Change at Max	SD at Max (%)
47	anti–DR5-Cy5 antibody (3rd dose)	Mice	pcFluc-DEVD	Monotonic	N/A	8	4.21	172.2
47	anti–DR5-Cy5 antibody (subcutaenous tumor)	Mice	pcFluc-DEVD	Unimodal	46.2	8	11.87	56.6
29	Docetaxel	Mice	Z-DEVD-aminoluciferin	Monotonic	N/A	72	3.05	NR
48	Irinotecan	Mice	Z-DEVD-aminoluciferin	Unimodal	35.2	24	2.02	9.8
48	Temozolimide	Mice	Z-DEVD-aminoluciferin	Monotonic	N/A	48	2.13	38.7
Median (Unimodal Responses) Overall					**27.7**	**24**	**1.99**	
Median (Unimodal Responses) Human					**14.1**	**4**	**3.7**	
Median (Unimodal Responses) Rodent					**31.5**	**24**	**1.89**	

Two FWHM values are provided for the bimodal models. FC: flow cytometry, NR: not reported.